Supporting Information

Achieving Reversible Zn Chemistry by Constructing a Built-in Internal Electric Field to Dynamically Eliminate the Local Charge Accumulation

Xueru Yang, Zhaoyu Zhang, Yufei Zhang, Wencheng Du, Minghui Ye, Yongchao Tang, Zhipeng Wen, Xiaoqing Liu, and Cheng Chao Li**

Experimental Sections

Chemicals

NaOH (AR), $[\text{-}CH_2CHOH\text{-}]_n$ (PVA 1788, 87.0~89.0% (mol/mol), $(C_8H_{16}ClN)_n$ (PDDA, 20wt.% in water), I_2 (99.8%), NH_4VO_3 (99%), $H_2C_2O_4 \cdot 2H_2O$ (≥99.5%), $ZnSO_4 \cdot 7H_2O$ (AR) and C_5H_9NO ((>99.0%) were purchased from Aladdin (Shanghai, China). $C_2H_3ClO_2$ (99%) was purchased from Energy Chemical. HCl (AR) was purchased from Guangzhou Chemical Reagent Factory. CH_3CH_2OH (Alcohol) was purchased from Damao Chemical Reagent Factory. $[C_6H_7O_2(OH)_2OCH_2COONa]_n$ (CMC) was purchased from Lizhiyuan battery sales department. Zn foil (99.95%) and Cu foil (99.95%) were purchased from Canrd new energy. Such chemicals were used as received.

Preparation of Electrolytes

The 2 M $ZnSO_4$ electrolytes were prepared by dissolving $ZnSO_4 \cdot 7H_2O$ into deionized water (DI).

Preparation of Materials

Synthesis of CMPVA powders: The carboxymethylated polyvinyl alcohol (CMPVA) was synthesized by reacting polyvinyl alcohol with haloacetic acid under

basic condition. 3 g PVA 1788 was poured into the NaOH solution and stirred overnight, then 6.5 g $C_2H_3ClO_2$ (dissolved in 5 mL DI) was added and magnetically stirred at 70 °C for 4h. The CMPVA was collected and washed with alcohol several times, and vacuum dried at 60 °C for 24 h to obtain CMPVA powder.

Synthesis of Zn@CP electrode: The Zn@CP electrode was prepared by solution casting process. Specifically, CMPVA powder was dissolved in DI at 85°C for 12h in the mass ratio of 1:9. Commercial PDDA was added and mixed thoroughly with magnetic stirring to obtain a slurry. Then the slurry was pasted onto a Zn foil by using a doctor-blading method. The Zn@CP electrode was obtained after drying at 60°C for 24h in the vacuum oven.

Preparation of PAC-I_2 cathode: The PAC-I_2 cathode was prepared through a solution-adsorption method. Typically, commercial I_2, activated carbon, carbon black and CMC were mixed thoroughly in DI solvent in the mass ratio of 4:4:1:1 with magnetic stirring to obtain a slurry. Then the mixture was casted onto a graphite paper. The PAC-I_2 cathode was obtained after drying for 12h in the air at 60°C. The average areal loading of I_2 was about 2.5-3 mg cm^{-2} in the electrode.

Synthesis of $NH_4V_4O_{10}$: 1.170 g NH_4VO_3 was dissolved in DI (70 mL) to obtained a light yellow solution. Subsequently, 1.891 g $H_2C_2O_4 \cdot 2H_2O$ was added int the solution under magnetically stirring, then transferred into autoclave at 140°C for 48h. The $NH_4V_4O_{10}$ was collected and washed with DI several times. The $NH_4V_4O_{10}$ powder was obtained after drying at 60°C for 12h in the vacuum oven.

Preparation of $NH_4V_4O_{10}$ cathode: The $NH_4V_4O_{10}$ cathode was prepared through a solution-adsorption method. Typically, $NH_4V_4O_{10}$, carbon black and polyvinylidene fluoride (PVDF) were mixed thoroughly in N-methyl-2-pyrrolidone (NMP) solvent in the mass ratio of 7:2:1 with magnetic stirring to obtain a slurry. Then the mixture was cast on a stainless steel wire mesh. The $NH_4V_4O_{10}$ cathode was obtained after drying at 80 °C for 12 h in the vacuum oven.

Material Characterizations

FT-IR spectra were obtained by an FT-IR spectrometer (Nicolet iS5, Thermo Scientific). Raman spectra were collected by using a Raman spectrometer (LabRAM HR Evolution, HORIBA JY). SEM images were taken by field emission scanning electron microscope (SU8220, Hitach, Japan). Atomic force microscope (AFM) images were acquired under tapping mode on a Dimension FastScan (Bruker). XRD patterns obtained by X-ray diffractometer (D8 VENTURE, Bruker, Germany). Contact angle measurements were performed on the OCA 100 (Dataphysics) contact angle meter. Microstructures were imaged using a confocal microscope (Carl Zeiss LSM800 with Airscan). The electron backscatter diffraction (EBSD) results of the zinc anode were characterized by a field-emission scanning electron microscopy (Apreo 2S HiVac, Thermo Scientific). Before the EBSD test, the zinc anode was processed with an polisher (VibroMet, Buehler).

Simulation methods

Density Functional Theory (DFT) calculations were conducted using the Vienna Ab-initio Simulation Package (VASP) 5.4 code, employing the Perdew-Burke-Ernzerhof generalized gradient approximation functional and projected augmented wave pseudopotentials with a 500 eV energy cutoff. Γ-point k-point sampling was utilized for all calculations. Geometry relaxations were carried out until the total force on each ion was reduced below 0.05 eV/Å.

Ab Initio Molecular Dynamics (AIMD) simulations were employed, leveraging one of the significant advantages of AIMD, where forces acting on the nuclei are directly computed from electronic states, and the many-body Schrödinger equation is solved at each time step. It is noteworthy that the computational demands of AIMD are substantial, limiting the number of atoms feasible for analysis in the model. The model consists of Zn atoms forming the base layer, with H_2O and SO_4^{2-} on the surface. There are 668 atoms in the system without polymer attachment and 798 atoms with polymer attachment. The AIMD simulations were conducted for a total duration of 50 ps, employing time steps of 2 fs. This comprehensive approach provides a detailed

understanding of the system's dynamics and properties, with particular attention to the interactions at the atomic level.

COMSOL simulations were employed, using secondary current distribution and dilute substance transfer module. The Bulter Volmer equation was used for calculation in simulation and the electric field distribution of the structure can be obtained through simulation analysis. The formula is as follows:

$$I = I_0\left[exp\left(\frac{\beta\eta F}{RT}\right) - exp\left(\frac{-\alpha\eta F}{RT}\right)\right]$$

Among them, I is the local current density; I_0 is the exchange current density; η is the magnitude of the overpotential; F is the Faraday constant; α is the cathode transfer coefficient; β is the anode transfer coefficient; R is the ideal gas constant; T is the absolute temperature. According to the formula, the local current density is proportional to the overpotential, and the local current density increases exponentially with the increase of overpotential. Therefore, increasing the magnitude of overpotential can achieve an order of magnitude increase in local current density, thereby significantly improving the rate of electrochemical deposition reaction.

The Nernst Planck equation was used to calculate the concentration distribution of the structure, as follows:

$$J_i = J_{c,i} + J_{d,i} + J_{t,i} = vc_i - D_I\nabla c_i \pm c_i u_i E$$

Among them, J_i is the total mass transfer flux of i ion; $J_{c,i}$ is the convective flux of the i ion; v is the liquid flow rate on the electrode surface; c_i is the concentration of i ion; $J_{d,i}$ is the diffusion flux of i ion; D_i is the diffusion coefficient of i ion; ∇c_i Is the concentration gradient of i ion; $J_{t,i}$ is the electromigration flux of the i ion; U_i is the mobility of i ions; E is the strength of the electric field, and for positive and negative ions, the electromigration flux is marked with positive and negative signs, respectively. In addition, the upper boundary of the geometric model is set as the anode, and the lower boundary is set as the cathode. The anode potential is 0 V, the cathode potential is -0.6 V, and the electrolyte solution concentration is set to 2 M. There are a total of 10790 grid cells, with a minimum cell mass of 0.5414 and an average cell mass of 0.8174.

For the binding energy calculation by DFT, Gaussian09 E.01 software3 was used. The B3LYP-D34, 5 functional and def2-SVP6 basis set was used to optimize the geometries of molecules. The vibration analysis was performed at the same theoretical level to ensure that all structures are energy minima (0 imaginary frequency) and get the correction of Gibbs free energy. The high-precision single-point energy was calculated at the PBE0-D37 /def2-TZVP6 theoretical level. Solvent effects of water (ε = 78.4) or DMSO (ε = 47.2) were considered by SMD8 solvation model and the solvation free energy was calculated at M052X9 /6-31G(d)10-13 level. The restrained electrostatic potential14 (RESP) atom charges and electrostatic potential (ESP) were calculated by Multiwfn15, 16 software.

The binding energy ($E_{binding}$) between cation and anion group is defined as follows:

$$E_{binding} = E_{complex} - E_{cation} - E_{anion}$$

Where $E_{complex}$ is the total energy of cation and anion complex, E_{cation} is the energy of cation, E_{anion} is the energy of anion. The electrostatic potential (ESP) was analyzed and plotted by the graphical interface of GaussView5.0.

Electrochemical Measurements

For the assembly of Zn//I_2 full cell, the positive electrode was prepared with 40 wt% I_2 as active material, 50 wt% carbon as conductive agent, and 10 wt% CMC as binder. Electrochemical performances were evaluated using CR2032 coin-type cells, and the I_2 loading mass of the electrodes was 2.5~3 mg cm^{-2}. The low N/P ratio batteries were assembled using 10-μm Zn foil. Otherwise, unless stated, the anode was metallic Zn foil of 100 μm thickness and Whatman GF/D glass microfibers papers served as the separators. The Zn//$NH_4V_4O_{10}$ full cell was assembled in the same process as Zn//I_2, except that the positive electrode was prepared with 70 wt% $NH_4V_4O_{10}$ as active material, 20 wt% carbon black as conductive agent, and 10 wt% PVDF as binder. The galvanostatic discharge/charge tests were measured on a Neware battery testing system (CT-4008-5V6A, Shenzhen, China) at room temperature. The cyclic voltammetry (CV) curves, corrosion curves, linear sweep voltammetry (LSV) curves, chronoamperometry curves, and linear polarization (Tafel) curves were obtained on a Gamry

electrochemical workstation with a three-electrode system (Zn foil as work electrode, Pt as counter electrode, and Ag/AgCl as reference electrode). Zn||Cu and Zn||Zn symmetric cells were assembled to evaluate the CE and cycling durability of Zn anodes in different electrolytes using CR2032 coin-type cells.

Capacity and energy density calculation

The capacity of Zn//I_2 full cells is evaluated by the specific capacity of I_2 cathode according the following formula:

$$C = \frac{It}{m}$$

where C is the specific capacity (mAh g^{-1}), I is the applied current (mA), t is discharge time (h), and m is the mass of the active material (g), which denoted as the mass of iodine in the bulk cathode.

The specific energy density of Zn//I_2 full cells is calculated based on the following equation:

$$E_g = \int_{V_0}^{V_1} C_g(V)$$

Where Eg is the calculated specific energy density (W h kg-1), V0 and V1 are the voltage lower limit and voltage upper limit of the discharge procedure, respectively; C_g is the specific capacity.

The volumetric energy density is calculated based on the following equation:

$$E_v = \int_{V_0}^{V_1} C_v(V)$$

Where Ev is the calculated specific volumetric density (W h L-1), V0 and V1 are the voltage lower limit and voltage upper limit of the discharge procedure, respectively; C_v is volumetric capacities calculated.

Mechnical properties measurments

The mechanical properties of the Zn@CP coating layer is characterized by AFM and nanoindentation techniques using peak force QNM™ mode. The plot of repulsion

force reflects from probe vs. probe indentation depth, namely force curve (Fig. 1h). The yellow line represents the probe approaches the sample surface (the highest point) and the blue line represents the probe retrace back to original point. The highest point represents the peak force where the probe reaches its bottom-most position. The lowest point represent the minimum force when the probe is withdrawing. Therefore, the lowest point relative to original point is the adhesion force. The slope of the rising section of yellow line represents elastic modulus fit using the Derjaguin–Muller–Toporov (DMT) model:

$$F_L(i) = \frac{4}{3}E^* \sqrt{R^*}\, i^{\frac{3}{2}} + F_{pull-off}$$

where FL is the load force, E* is the reduced Young's modulus E* = E/(1 − ν_2), ν is the Poisson ratio, R* is the reduced radius 1/R* = 1/Rindenter + 1/Rsurface , i is the indentation depth, and Fpull-off is the force at the point B of the AFM force curve, or the adhension force. The adhension force can easily be found from the force curves. Energy dissipation is given by the Force times the velocity integrated over one period of the vibration (represented by the dashed area in Fig. 1h)

as in Equation:

$$W = \int \vec{F} \cdot d\vec{Z} = \int_0^T \vec{F} \cdot \vec{v} dt$$

where W represents energy dissipated in a cycle of interaction. F is the interaction force vector and dZ is the displacement vector. Because the velocity reverses its direction in each half cycle, the integration is zero if the loading and unloading curves coincide. For pure elastic deformation there is no hysteresis between the repulsion parts (dashed parts) of the force curve, corresponding to very low dissipation. In this case the work of adhesion becomes the dominant contributor to energy dissipation. Energy dissipated is presented in electron volts as the mechanical energy lost per tapping cycle.

Results and Discussion

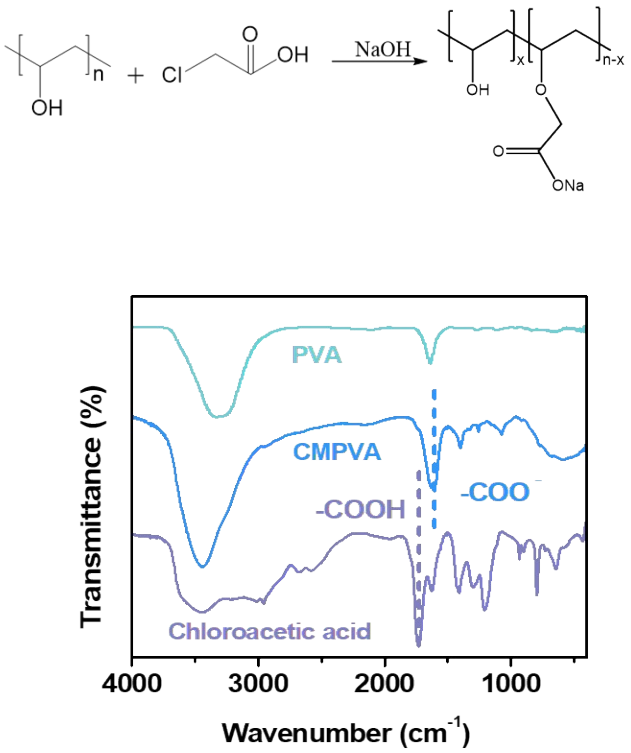

Fig. S1 Synthesis process of CMPVA (top). FTIR spectra of PVA, chloroacetic acid and the as-synthesized CMPVA (bottom).

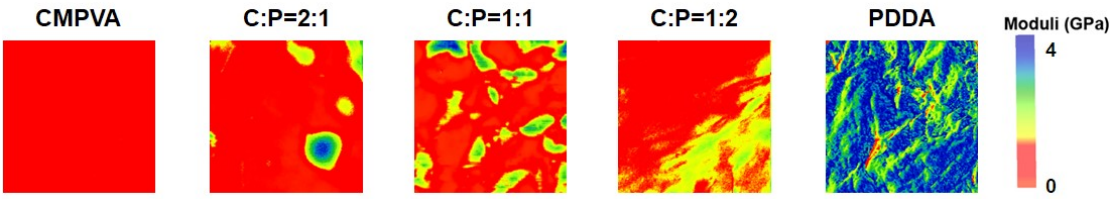

Fig. S2 Young's modulus mapping of the CP samples prepared with different ratios of CMPVA and PDDA. (C:P=1:1, C:P=2:1 and C:P=1:2 represents the volume ratio of CMPVA and PDDA is 1:1, 2:1 and 1:2, respectively). The results are tested by coating CP onto 100 μm Zn foil.

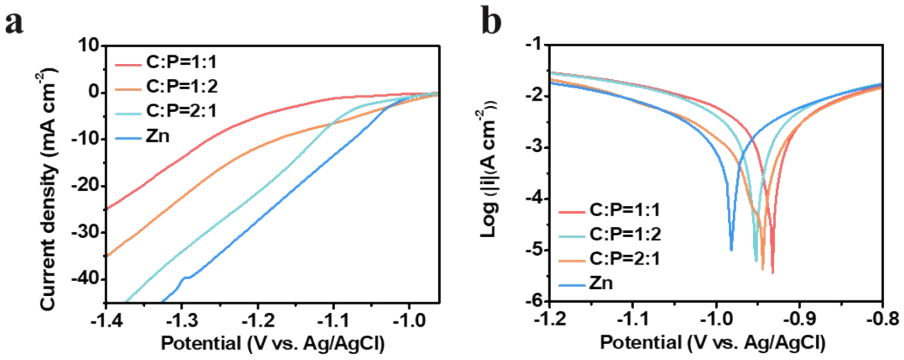

Fig. S3 (a) LSV curves and (b) Tafel plots of Zn anode protected by CP with different ratios of CMPVA and PDDA (C:P=1:1, C:P=2:1 and C:P=1:2 represents the volume ratio of CMPVA and PDDA is 1:1, 2:1 and 1:2, respectively).

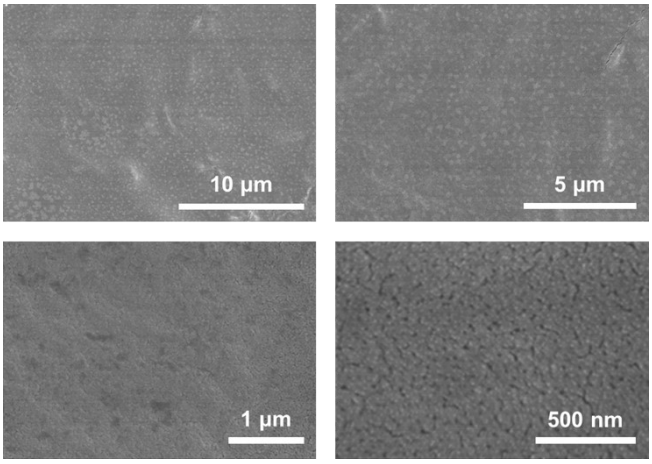

Fig. S4 SEM images of CP gel at different magnification scales.

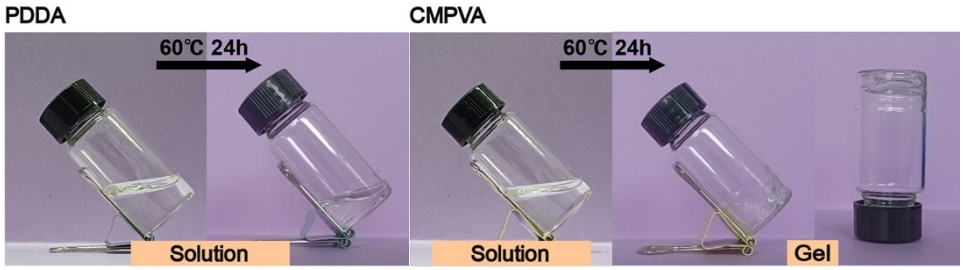

Fig. S5 Optical observation of drying process of PDDA solution and CMPVA solution.

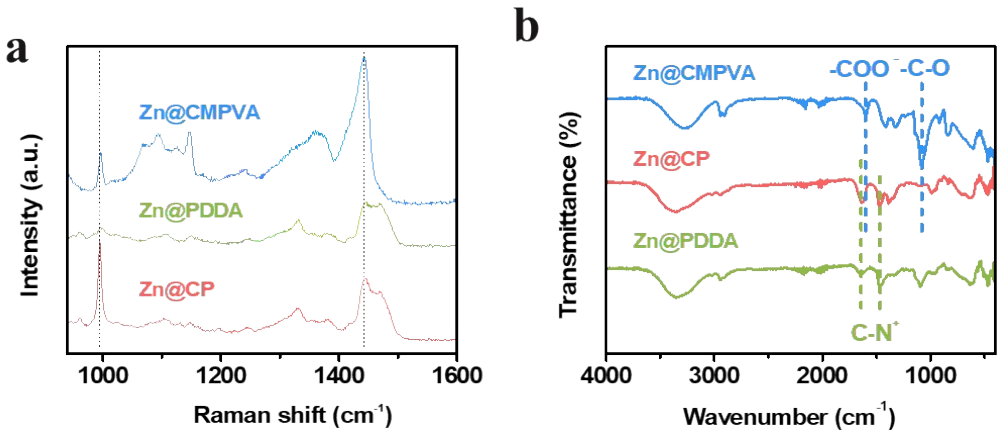

Fig. S6 (a) Raman and (b) FTIR spectra of Zn@CMPVA, Zn@CP and Zn@PDDA.

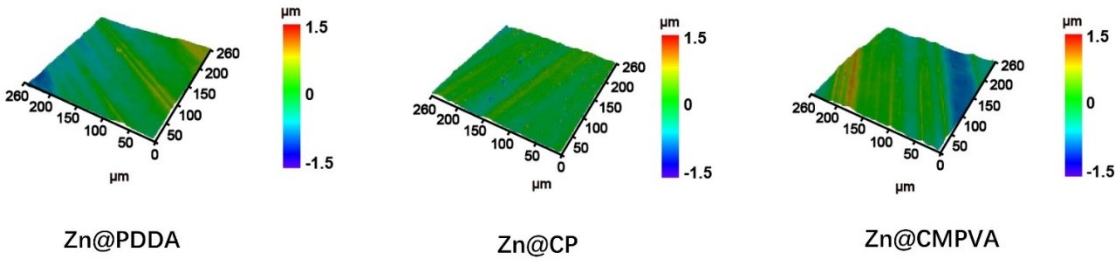

Fig. S7 3D morphology CLSM image of Zn@CMPVA, Zn@CP and Zn@PDDA electrodes.

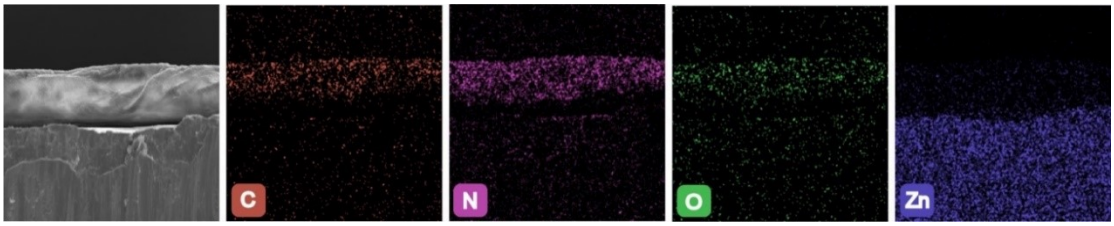

Fig. S8 Cross-sectional SEM image of Zn@CP and corresponding EDS mapping of C, N, O and Zn elements.

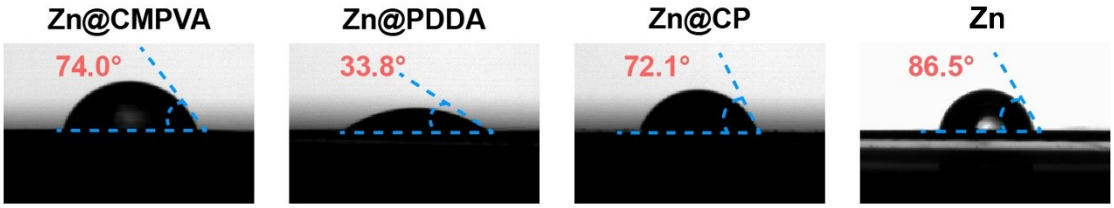

Fig. S9 Contact angles of Zn@CMPVA, Zn@PDDA, Zn@CP, and Zn.

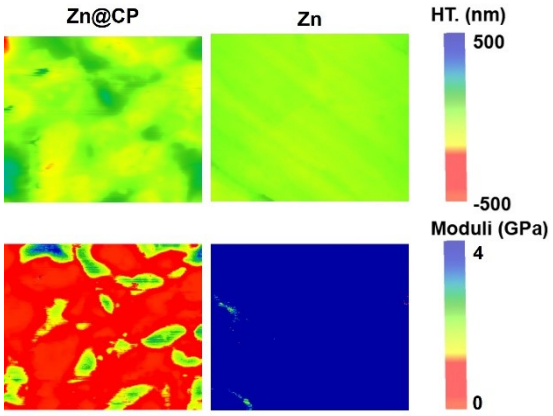

Fig. S10 Surface morphorlogy (top) and Young's modulus (bottom) map of Zn@CP and Zn.

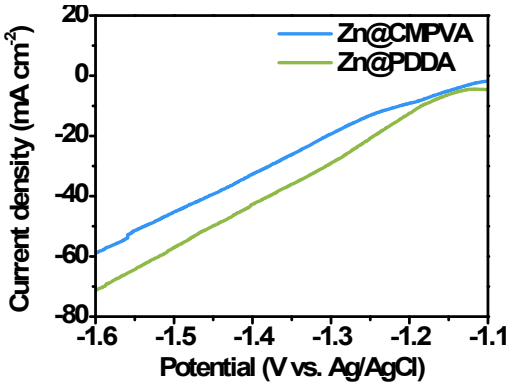

Fig. S11 LSV curves of Zn@CMPVA and Zn@PDDA.

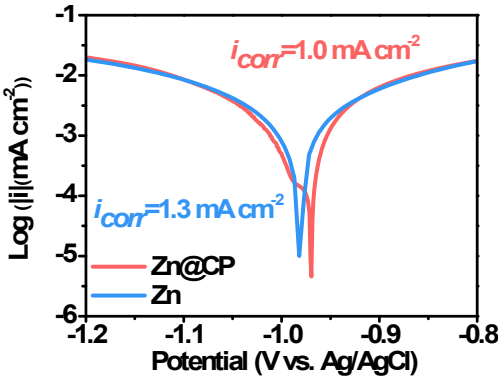

Fig. S12 Tafel plot of Zn@CP and Zn.

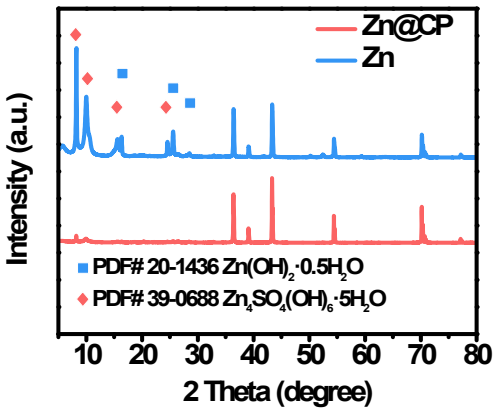

Fig. S13 XRD patterns of Zn@CP and Zn immersed in $ZnSO_4$ electrolyte for 7 days.

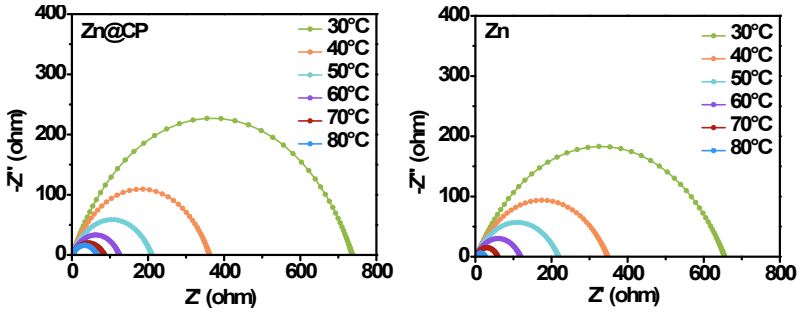

Fig. S14 Corresponding Arrhenius curves of Zn@CP and Zn.

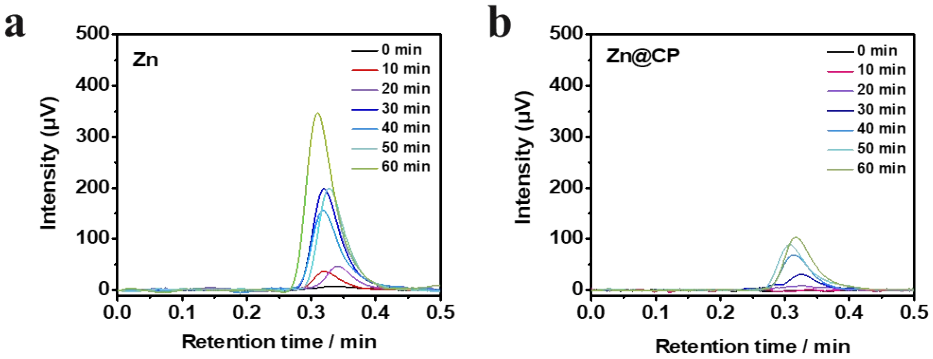

Fig. S15 In-situ GC profile for quantitative H_2 tracking during Zn plating at 1 mA cm^{-2} of (a) Zn and (b) Zn@CP anode.

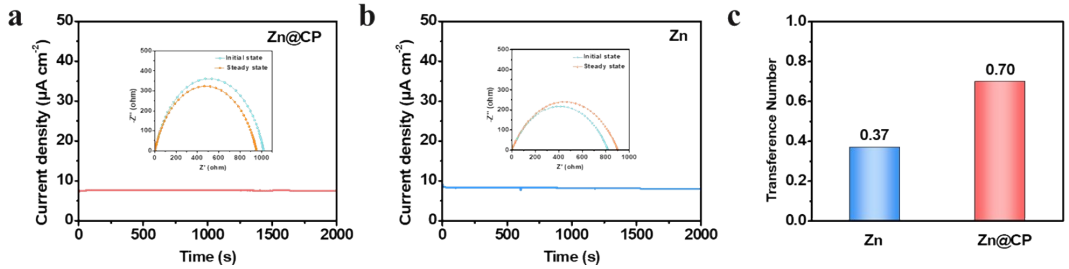

Fig. S16 Current–time curve and corresponding electrochemical impedance spectroscopy (EIS) spectra (inset) before and after the CA test (a) Zn@CP and (b) Zn in 2 M $ZnSO_4$. (c) Zn^{2+} transference number comparison of Zn and Zn@CP.

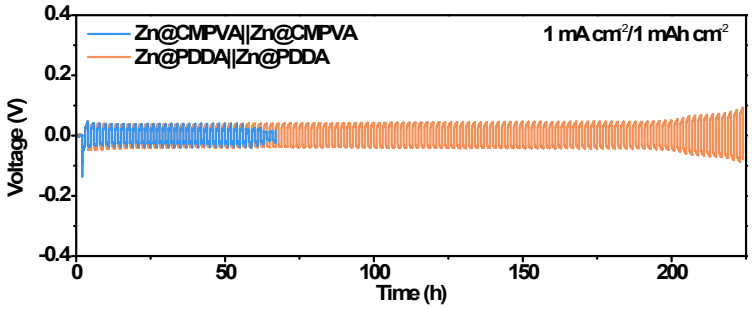

Fig. S17 Galvanostatic cycling performance of Zn@CMPVA||Zn@CMPVA and Zn@PDDA||Zn@PDDA cells.

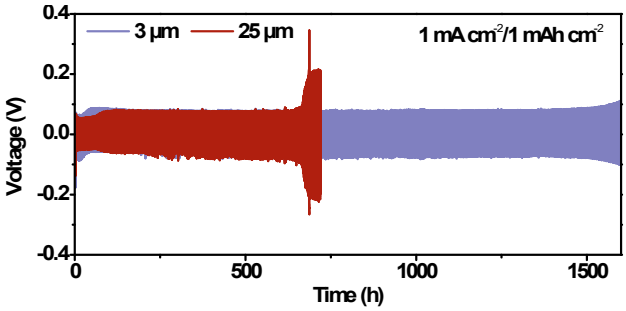

Fig. S18 Galvanostatic cycling performance of Zn@CP||Zn@CP cell with coating thickness of 3 µm and 25 µm.

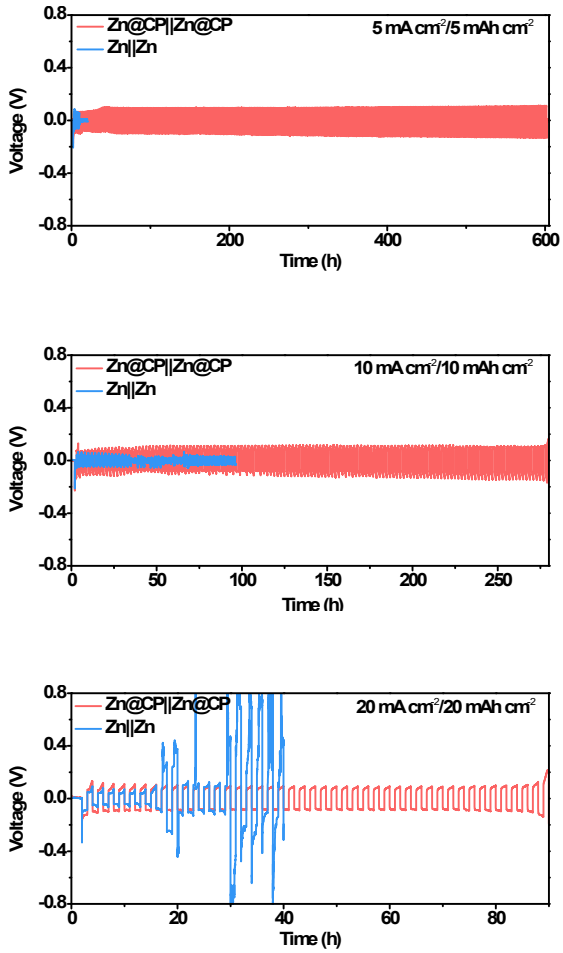

Fig. S19 Galvanostatic performance of Zn@CP||Zn@CP and Zn||Zn cells at 5 mA cm^{-2}/5 mAh cm^{-2} (top), 10 mA cm^{-2}/10 mAh cm^{-2} (middle) and 20 mA cm^{-2}/20 mAh cm^{-2} (bottom).

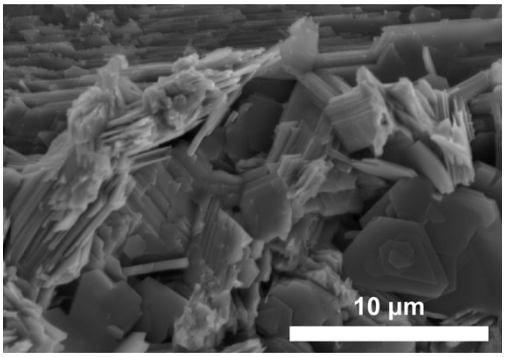

Fig. S20 Top-view SEM image of Zn deposits at cycle number of 50.

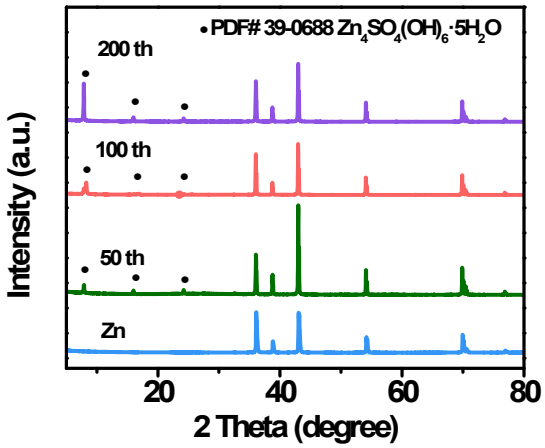

Fig. S21 XRD patterns of Zn deposits at different cycle numbers on Zn.

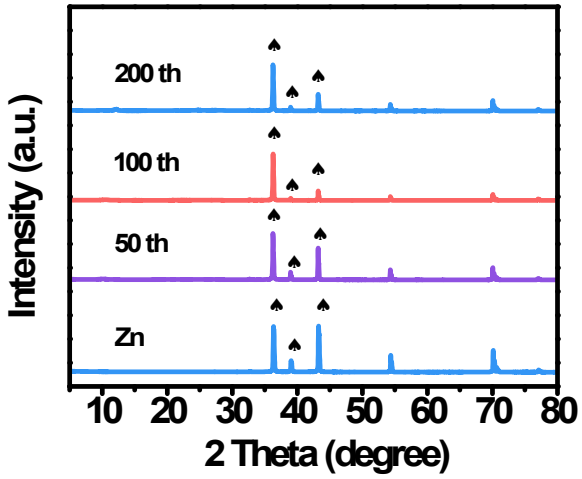

Fig. S22 XRD patterns of the Zn deposits at different cycle numbers on Zn@CP at stripping side.

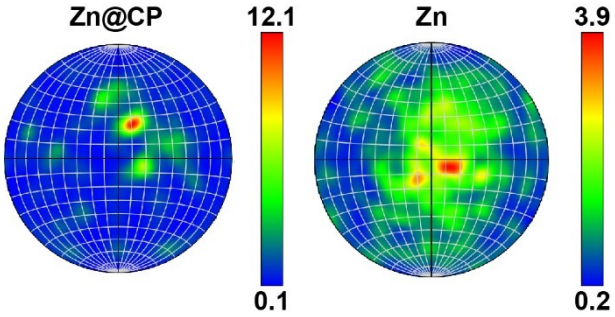

Fig. S23 The (002) plane pole figure of the cycled Zn@CP and Zn by EBSD.

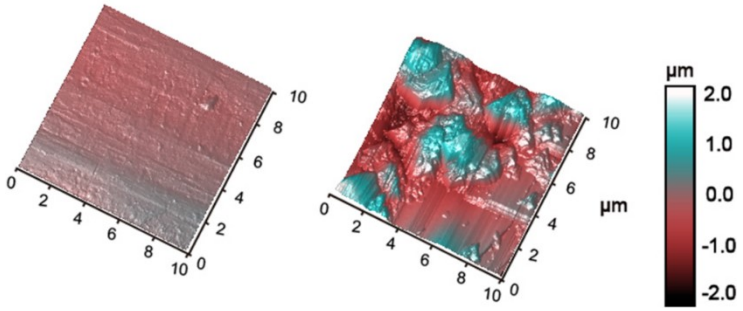

Fig. S24 3D morphology AFM images of Zn before (left) and after (right) 50 cycles at plating side.

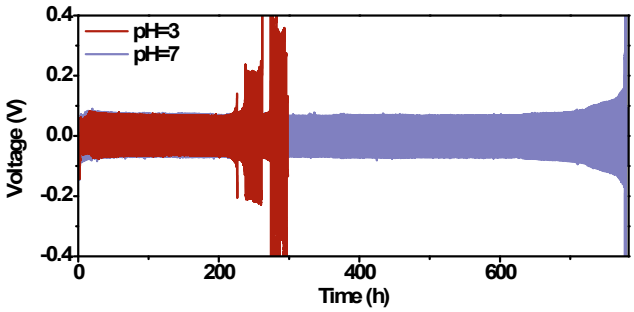

Fig. S25 Galvanostatic cycling performance of Zn@CP||Zn@CP cells with adjusted-pH CP coverage.

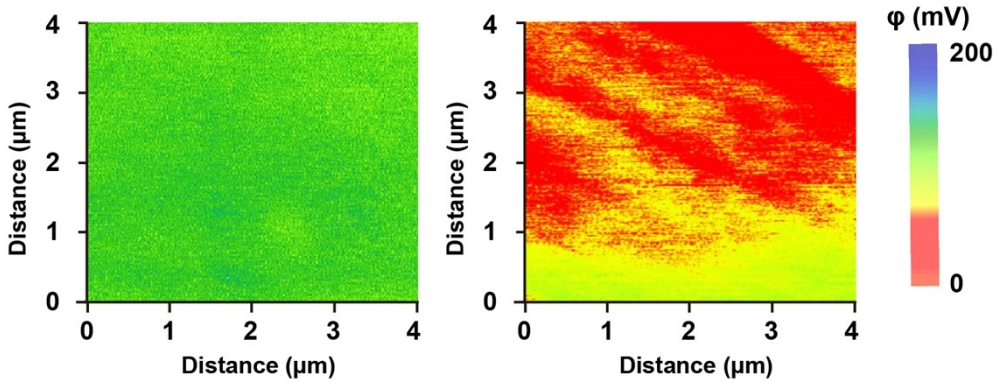

Fig. S26 Volta potential mapping of Zn@CP (left) and Zn (right) via KPFM.

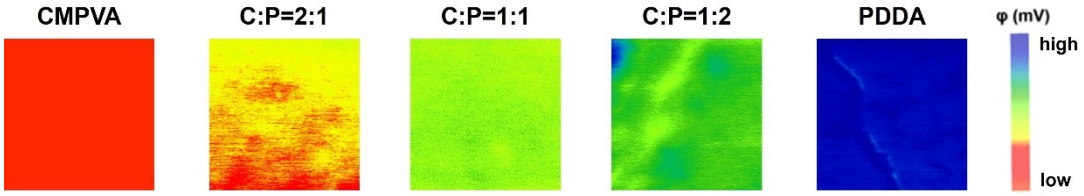

Fig. S27 Volta potential mapping of CP prepared by CMPVA and PDDA at different ratios via KPFM.

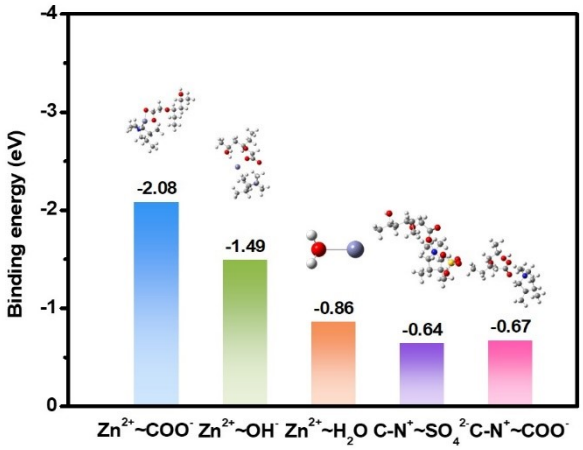

Fig. S28 Binding energy comparison of Zn^{2+} with COO^-, H_2O, OH^-, SO_4^{2-} and SO_4^{2-} with $C\text{-}N^+$.

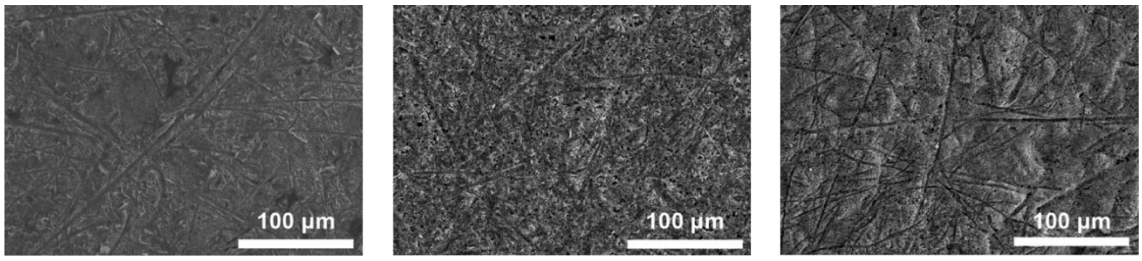

Fig. S29 Top-view SEM images of Zn@CP at different cycle numbers of 50 (left), 100 (middle) and 200 (right) at plating side.

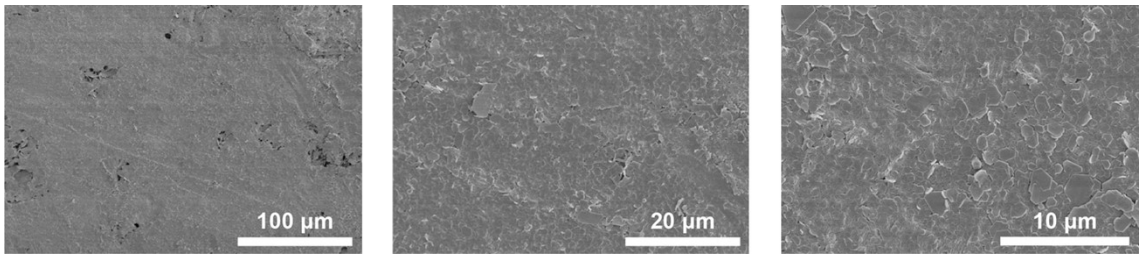

Fig. S30 Top-view SEM images of deposited Zn on Zn@CP at cycle number of 50 at stripping side.

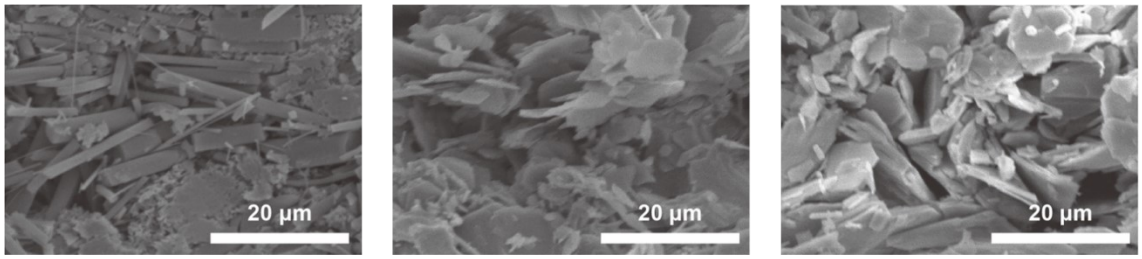

Fig. S31 Top-view SEM images of deposited Zn on Zn at different cycle number of 50 (left), 100 (middle) and 200 (right) at plating side.

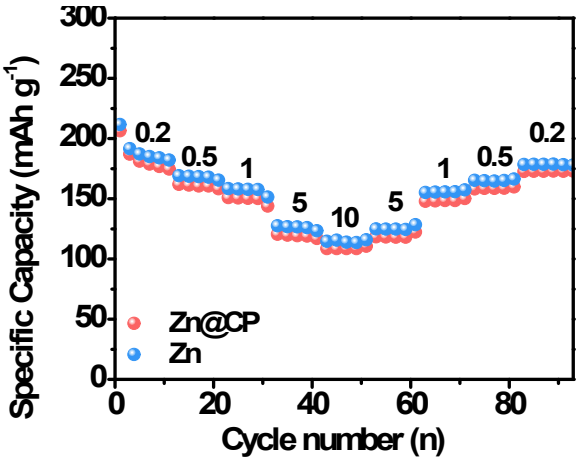

Fig. S32 Rate capability performance of Zn@CP||I_2 and Zn||I_2 full cells.

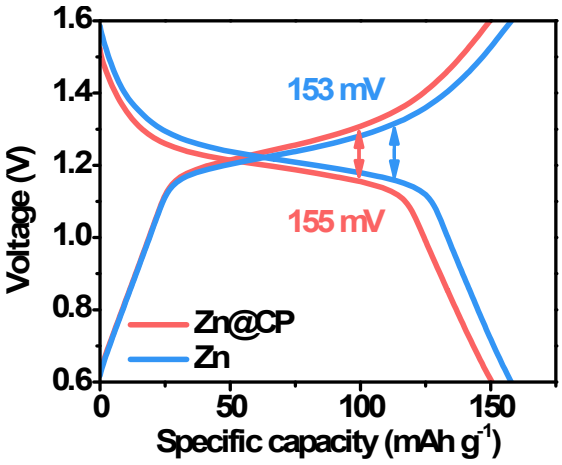

Fig. S33 Capacity-voltage profiles of Zn@CP||I_2 and Zn||I_2 full cells. The slightly lower capacity of Zn@CP||I_2 than that of Zn||I_2 should be attributed to the increased impedance of CP at the anode.

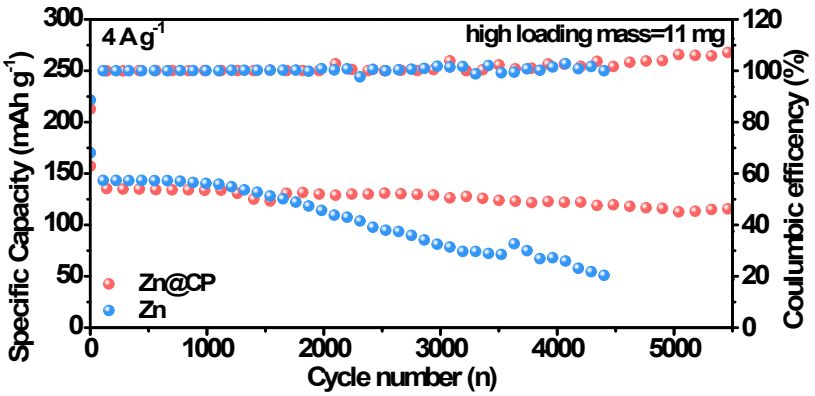

Fig. S34 Cycling stability of Zn@CP||I_2 and Zn||I_2 full batteries. The slightly lower capacity of Zn@CP Zn@CP||I_2 than that of Zn||I_2 should be attributed to the increased impedance of CP at the anode.

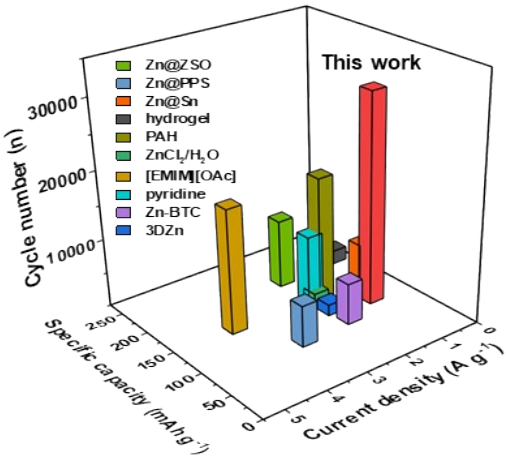

Fig. S35 The energy density comparison of Zn@CP||I_2 and other reported Zn anodes with SEI modification.

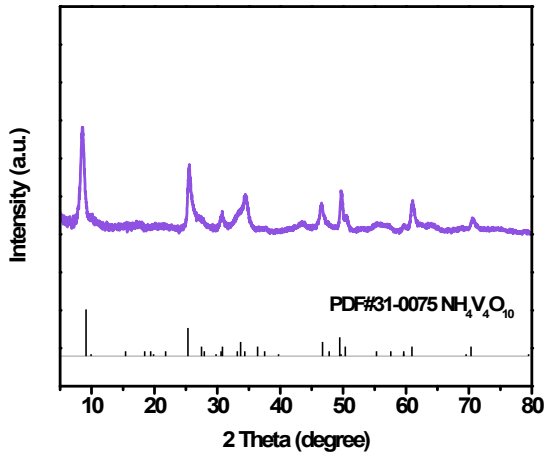

Fig. S36 XRD patterns of $NH_4V_4O_{10}$.

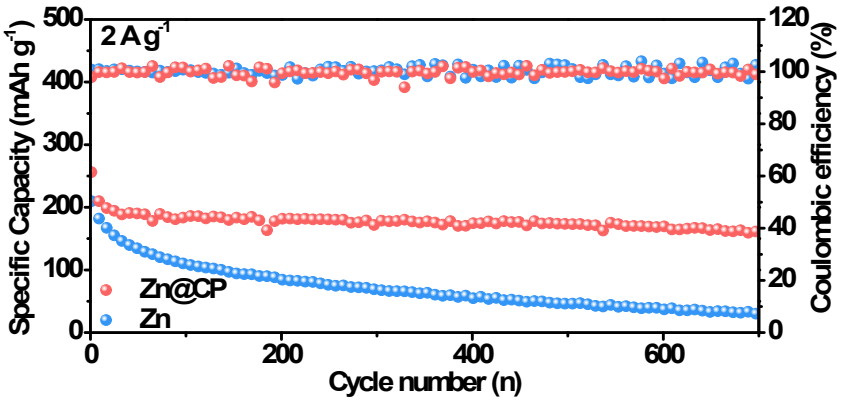

Fig. S37 Cycling stability of Zn@CP||$NH_4V_4O_{10}$ and Zn||$NH_4V_4O_{10}$ full cells.

Table 1. The specific and volumetric energy densities of Zn@CP//I_2 and Zn//I_2 calculated from I_2 cathode (Fig. 6c).

Sample	Status	Specific capacity	Volumetric capacity
Zn@CP//I_2	Initial	139.94 Wh kg^{-1}	101.32Wh L^{-1}
	18000 cycles	128.52 Wh kg^{-1}	93.05 Wh L^{-1}
Zn//I_2	Initial	160.12 Wh kg^{-1}	115.93Wh L^{-1}
	18000 cycles	90.52 Wh kg^{-1}	65.54 Wh L^{-1}